RSC Advances

PAPER

View Article Online
View Journal | View Issue

Cite this: *RSC Adv.*, 2019, **9**, 15033

Highly effective photocatalytic performance of {001}-TiO_2/MoS_2/RGO hybrid heterostructures for the reduction of Rh B†

Ya Gao,[a] Yongjie Zheng,*[a] Jixing Chai,[b] Jingzhi Tian,[a] Tao Jing,[a] Deqing Zhang,[b] Junye Cheng,*[c] Huiqing Peng,[c] Bin Liu*[c] and Guangping Zheng[d]

Effective separation and rapid transfer of photogenerated electron–hole pairs are key features of photocatalytic materials with high catalytic activity, which could be achieved in co-catalysts. It is reported that the two-dimensional (2D) MoS_2 is a promising co-catalyst due to its unique semi-conductive properties and graphene-like layered structure. However, the application of MoS_2 as a co-catalyst is limited by its poor electrical conductivity. On the other hand, it is worth noting that TiO_2 possesses reactive crystal facets, which is one of the dominant mechanisms for the separation of photogenerated electron–hole pairs. In this work, we prepared MoS_2/RGO hybrids as co-catalysts which were doped to TiO_2 with highly reactive {001} planes *via* the hydrothermal method. It was found that the {001}-TiO_2/MoS_2/RGO photocatalysts with 7 wt% MoS_2/RGO co-catalyst show the highest photodegradation activity for the degradation of Rh B under visible light irradiation (λ > 400 nm), which could result from the synergy of the effective separation of electron–hole pairs by the {001} facets in TiO_2 and the rapid transfer of electron–hole pairs in MoS_2/RGO. The results show that the {001}-TiO_2/MoS_2/RGO hybrid is a low-cost and stable photocatalyst for the effective degradation of Rh B under visible light.

Received 8th April 2019
Accepted 8th May 2019

DOI: 10.1039/c9ra02634g

rsc.li/rsc-advances

1. Introduction

Semiconducting photocatalysts exhibit great prospects in the removal of pollutants from water and air.[1–4] Among the pursued semiconductors, titanium dioxide (TiO_2) with a band gap of 3.2 eV between the conduction band (CB) and valence band (VB), has attracted attention as a photocatalytic material owing to its nontoxicity, chemical stability, low cost, high chemical inertness.[5–10] The active photocatalytic characteristics of TiO_2 are restricted due to the rapid recombination of photogenerated electron–hole pairs.[11,12]

There are two strategies that have been carried out to enhance the photocatalytic performance of TiO_2. One of the strategies is based on the design of unique morphology and structure of TiO_2, such as mesoporous TiO_2 hollow shells,[13,14] TiO_2 nanosheet arrays,[15,16] and three-dimensional network TiO_2 nanowire films.[17] Another strategy is the loading of co-catalyst, including graphene (GN),[18–20] metallic phases[21,22] and nonmetallic phases[23,24] of materials, as well as polymer-metallic catalysts.[25,26] Zhang *et al.*[20] reported a successful strategy to improve the photocatalytic performance of TiO_2 *via* introducing the GN without defects to enhance the interfacial contact between GN and TiO_2; Liu *et al.*[22] prepared Ag/Ag(I)–TiO_2 photocatalyst by a facile impregnated method in combination with a calcination process and the photocatalyst showed a higher visible-light photocatalytic activity; Qu *et al.*[24] synthesized a S,N co-doping GQD/TiO_2 composite though a facile hydrothermal and its photocatalytic performance (degradation of Rh B under visible light) was 10 times higher than that of P25; Jiang *et al.*[26] reported a nanostructured TiO_2 thin film accompanying with the effects of polymer conjugation and Mo-doping, as a result, the methylene blue dye degradation rate reached 90.6%. In the aforementioned methods, heterostructure photocatalysts consisting of two semi-conductive materials with different band gaps and electronic structures have been proved to be effective in photocatalysis.[27–31]

If developed into a co-catalyst material, MoS_2 have some particular advantages due to its graphene-like nanostructures, relatively high activity and unique semiconducting properties.[32–34] And there are numerous reports about MoS_2-based heterostructure for photocatalytic production of H_2. However the applications of MoS_2 in the removal of pollutants are limited by its poor electrical conductivity.[35–37] Generally, there

[a]School of Chemistry and Chemical Engineering, Qiqihar University, Qiqihar 161006, China. E-mail: yongjiezheng@163.com

[b]School of Materials Science and Engineering, Qiqihar University, Qiqihar 161006, China

[c]Center of Super-Diamond and Advanced Films (COSDAF), Department of Materials Science and Engineering, City University of Hong Kong, Hong Kong 999077, China. E-mail: binliu@mail.ipc.ac.cn; jycheng4-c@my.cityu.edu.hk

[d]Department of Mechanical Engineering, The Hong Kong Polytechnic University, Hung Hom, Kowloon, Hong Kong, China

† Electronic supplementary information (ESI) available. See DOI: 10.1039/c9ra02634g

are two synthesis routes in the fabrication of MoS_2-based heterostructure with effective charge transfer processes. First, chemical lithium intercalation could induce a phase change in MoS_2 from the 2H (showing semiconducting properties) to the 1T (showing metallic properties) phases, resulting in the heterostructure. Bai *et al.*[38] firstly reported that compared with (2H) MoS_2–TiO_2, the (1T) MoS_2–TiO_2 exhibits excellent photocatalytic performance. Second, the introduction of conductive materials into MoS_2 leads to a heterostructure. Peng *et al.*[39] synthesized MoS_2/RGO/CdS as an effective photocatalyst which can reduce and detoxify nitroaromatic compounds. The MoS_2-based heterostructures prepared by these two methods have played an important catalytic role, while the latter is more favorable because of its simplicity and efficiency.

Moreover, it is reported that the reactive crystal facets of TiO_2 are closely related with its photocatalytic efficiency, and the {001} facet-dominated single-crystal anatase TiO_2 shows higher photocatalytic activity than P25.[40–42] Enlightened by the above-mentioned findings, it is suggested that the {001}-TiO_2/MoS_2/RGO should be an ideal photocatalyst. In this work, we prepared a {001}-TiO_2/MoS_2/RGO hybrid photocatalyst with low cost. The as-prepared {001}-TiO_2/MoS_2/RGO exhibited more outstanding photocatalytic performance for the degradation of Rhodamine B (Rh B) under visible light irradiation ($\lambda > 400$ nm), compared with the pure {001}-TiO_2 and {001}-TiO_2/MoS_2. The enhanced photocatalytic activity could be ascribed to the effective charge separation and transfer due to the band gap of MoS_2 and high conductivity of graphene.

2. Experimental

2.1 Materials

All chemicals were in analytical grade and used without further purification. Molybdic acid ($H_2MoO_4 \geq 85\%$) was purchased from Shanghai Aladdin Biochemical Technology Co. Ltd. Thiourea (CH_4N_2S) was purchased from Tianjin Fuchen Chemical Reagent Factory. Graphene oxide dispersion were purchased from Nanjing Pioneer Nano Material Technology Co., Ltd. *N*-Butyl titanate (TBOT) was purchased from Tianjin Tianli Chemical Reagent Co. Ltd. Hydrofluoric acid (HF) was purchased from Tianjin Fuyu Chemical Reagent Co. Ltd.

2.2 Synthesis of {001}-TiO_2 nanosheets

The {001}-TiO_2 nanosheets were prepared by a simple hydrothermal route. Firstly, 25 ml of *n*-butyl titanate and 3 ml of hydrofluoric acid were added into a 100 ml Teflon-lined autoclave, under magnetic stirring for 2 h. After heating and stirring for 24 h at 180 °C, the solution was naturally cooled to room temperature and washed with deionized water and ethanol for several times until its pH value reached 7 and dried at 60 °C in a vacuum oven to obtain the {001}-TiO_2 nanosheets.

2.3 Synthesis of {001}-TiO_2/MoS_2/RGO hybrid

The nanohybrids were also prepared by a hydrothermal method. Firstly, the as-prepared MoS_2/RGO (with 7 wt% RGO) which was prepared by a one-step hydrothermal method previously reported,[43] was dispersed in 80 ml of DI. Secondly, 0.99 g of the as-prepared {001}-TiO_2 nanosheets were added to the above-mentioned dispersions. After subjected to magnetic stirring for 1 h, the mixture was transfer to a 100 ml Teflon-lined autoclave. After reaction for 3 h at 180 °C, the solution was naturally cooled down to the room temperature. Then the {001}-TiO_2/MoS_2/RGO hybrid was washed with deionized water and ethanol for several times and dried at 60 °C in a vacuum oven. With the same method described above, the {001}-TiO_2/MoS_2/RGO samples with different MoS_2/RGO loadings were prepared. The aforementioned facile synthesis route was summarized in Scheme 1.

2.4 Characterization

The morphology of samples was characterized by the field emission scanning electron microscope (SEM, Hitachi S-3400) and transmission electron microscope (TEM, Hitachi H7650). The crystallization properties were measured by X-ray powder diffraction (XRD) patterns (Bruker D8) with a Cu-Kα radiation. The crystal structure was observed with the high-resolution electron microscopy (HRTEM, Tecnai F30). Element information was characterized by X-ray photoelectron spectrometer (ESCALAB250Xi, Thermofisher Co). Raman spectrum was measured by the equipment Lab RAM HA Evolution. Ultraviolet-visible (UV-vis) absorption spectra were performed using a spectrophotometer (Lambda 35, American). The photoluminescence spectra (PL) was examined with a fluorescence spectrophotometer (RF-5301PC, Shimadzu Corporation, Japan). The information on the Brunauer–Emmett–Teller (BET) surface areas of the sample powders was obtained on an automatic gas adsorption analyzer (Conta Instruments, USA).

2.5 Evaluation of photocatalytic activity

The photocatalytic activities of the catalysts were evaluated through the degradation of Rh B under a light source of 300 W Xe arc lamp equipped with a cut-off filter ($\lambda > 400$ nm) for visible light. Firstly, 50 mg of photocatalyst was added into 50 ml Rh B solution (1 mg ml^{-1}). Then, the suspensions were stirred in dark for 30 minutes to reach the adsorption–desorption equilibrium. Third, the suspensions were subjected to the illumination every 10 minutes; in the intervals of illumination 5 ml suspension was withdrawn and centrifuged to remove the photocatalyst particles and then was tested by a UV-vis spectrophotometer to determine the concentration of Rh B through measurements on the 554 nm absorption peak. The Rh B concentration after adsorption equilibrium is regarded as the initial concentration (C_0).

3. Results and discussion

3.1 Results of characterization

The crystal structures of the prepared samples are characterized determined by XRD, and the XRD patterns of pure {001}-TiO_2, MoS_2/RGO and {001}-TiO_2/MoS_2/RGO are shown in Fig. 1a. The diffraction peaks at $2\theta = 25.28°$, 37.8°, 48.04°,

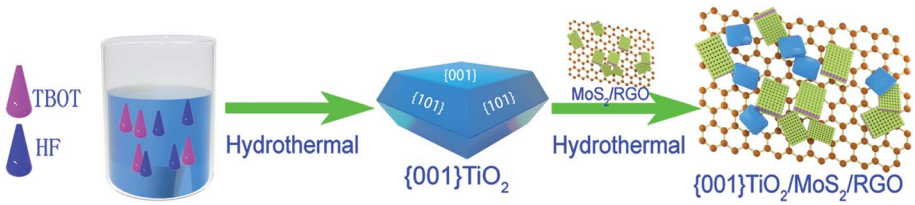

Scheme 1 Synthetic routes for the {001}-TiO_2 nanosheets and the {001}-TiO_2/MoS_2/RGO composites.

53.89°, 55.06°, 62.68°, 68.76°, 70.30°, 75.02°, 76.01° and 82.65° can be observed in {001}-TiO_2 and {001}-TiO_2/MoS_2/RGO samples, which are assigned to (101), (004), (200), (105), (204), (116), (220), (215), (301) and (224) planes of the anatase TiO_2 (PDF 21-1272), respectively. It is also seen that there are only two extremely weak peaks of the co-catalyst in the pattern for {001}-TiO_2/MoS_2/RGO (the inset in Fig. 1a). In the patterns for the MoS_2 and MoS_2/RGO samples (Fig. S1a†), there are four peaks at 2θ = 14.6°, 32.8°, 39.8° and 58.5°, which are assigned to (002), (100), (103), and (110) planes of MoS_2 (JCPDS37-1492), respectively. There are no obvious diffraction peaks for RGO mostly because of very small amount of RGOs in the samples.

To confirm the presence of RGO in the {001}-TiO_2/MoS_2/RGO hybrid, Raman measurements were carried out. Fig. 1b shows the Raman spectrum of {001}-TiO_2/MoS_2/RGO hybrid, it is observed that the weak $E_{g(1)}$, A_{1g} and $E_{g(2)}$ peaks for TiO_2 are located at 142.97 cm^{-1}, 515.22 cm^{-1} and 636.34 cm^{-1}, respectively. It also can be clearly observed that the E_{2g} and A_{1g} peaks for MoS_2 are located at 379.74 and 408.88 cm^{-1}, respectively. The peaks of the D- and G-band for RGOs are located at 1348.53 and 1588.53 cm^{-1}, respectively, and the I_{2D}/I_G ratio of RGO is 0.19 (0.07 < 0.19 < 0.3), suggesting that the hybrid have triple-layer graphene sheets.[43] The results of Raman spectra thus prove the presence of RGO in the hybrid.

The interactions between the TiO_2 and MoS_2/RGO in the {001}-TiO_2/MoS_2/RGO hybrid are studied by XPS spectra. As shown in Fig. 1c, the Mo, S, Ti, O, C and F elements appear in the survey spectrum. The peak at the binding energy of 684.5 eV is assigned to F 1s, which is a typical value for the fluorinated TiO_2 system such as the surficial Ti–F species.[44] Fig. 1d and S2a† shows the high-resolution spectra of Ti 2p for TiO_2 and {001}-TiO_2/MoS_2/RGO, respectively. The peaks located at the binding energies of 465.31 and 459.57 eV for TiO_2 could correspond to Ti $2p_{1/2}$ and $4p_{3/2}$, respectively, which can be assigned to a Ti^{4+} oxidation state. Compared with pure TiO_2, those peaks for {001}-TiO_2/MoS_2/RGO shift to 465.11 and 459.48 eV, indicating a strong interaction between MoS_2/RGO and TiO_2. As shown in the Mo spectrum of {001}-TiO_2/MoS_2/RGO (Fig. 1e), the bands located at the binding energies of 232.35 and 229.03 eV are assigned to Mo ($3d_{3/2}$) and

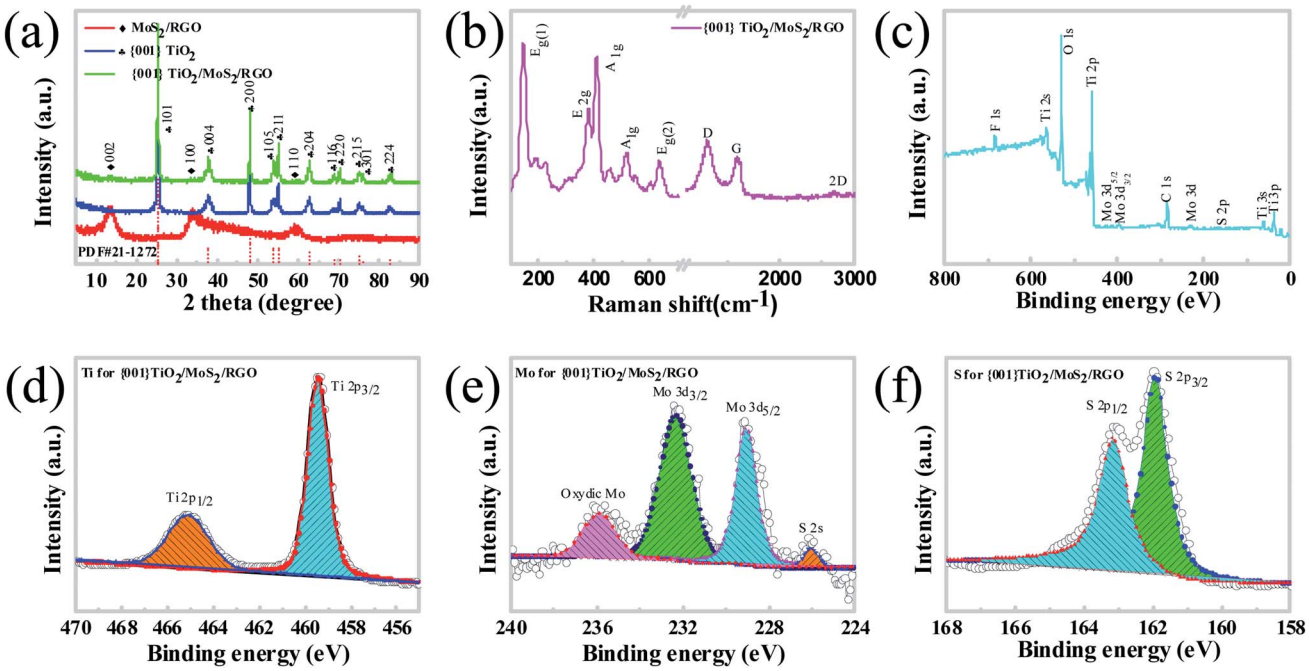

Fig. 1 (a) XRD patterns for MoS_2/RGO, {001}-TiO_2 and {001}-TiO_2/MoS_2/RGO, the inset is at 2θ = 5–45°; (b) Raman spectrum for {001}-TiO_2/MoS_2/RGO; (c) XPS survey spectrum for {001}-TiO_2/MoS_2/RGO; high-resolution spectra of {001}-TiO_2/MoS_2/RGO (d) Ti 2p; (e) Mo 3d; (f) S 2p.

Mo ($3d_{5/2}$) in the normal chemical state of Mo^{4+}, respectively. The S spectra of {001}-TiO_2/MoS_2/RGO are observed to have two peaks located at 162.82 and 161.71 eV, as shown in Fig. 1f, which are consistent with those of MoS_2. The C 1s spectrum can be deconvoluted into three peaks located at 288.75, 286.40, and 284.84 eV (Fig. S2b†), which correspond to the C=O, C–O, and C–C functionalities, respectively, and indicate the existence of the carboxy, epoxy, and hydroxyl groups in the graphene. The results indicate that most of the oxygen-containing functional groups are successfully removed. The reduction of GO to graphene will dramatically improve the electrical conductivity of the hybrids, and hence significantly enhancing their photocatalytic activity.[45,46]

Typical morphology and microstructure of the as-prepared catalyst are characterized using scanning electron microscopy (SEM). Fig. 2a shows that a large number of stacked MoS_2 nanosheets with significantly curled edges are observed. Fig. 2b shows the microstructure of MoS_2/RGO, indicating that the small MoS_2 nanosheets are well loaded onto the surfaces of RGOs. Fig. 2c shows the morphology of TiO_2, which exhibits a rectangular shape with lengths of about 40–60 nm. Fig. 2d show the morphology of {001}-TiO_2/MoS_2/RGO. No obvious MoS_2/RGO structures can be observed, which maybe caused by the low content of MoS_2/RGO. To determine the composition of {001}-TiO_2/MoS_2/RGO, the sample is measured by the energy dispersive spectrometer (EDS) as shown in Fig. S3.† Fig. S3† shows that there are a large amount of Ti and O elements, a small amount of Mo and S elements and a few C elements. Moreover, the distribution of Ti and O elements is even and consistent, and the Mo and S elements also show similar features of distribution. Thus, the EDS results demonstrate that the sample shown in Fig. 3d could be {001}-TiO_2/MoS_2/RGO.

Detailed microstructure of the samples can be clearly observed in the transmission electron microscopy (TEM) and high-resolution TEM (HRTEM). MoS_2 shows an appearance of thin nanosheets that look like soft and light flowers (Fig. 3b), for MoS_2/RGO hybrid, it can be clearly seen that the flower-like MoS_2 in the dark region is evenly attached to the bright and light RGOs (Fig. 3a and c). The {001}-TiO_2 has a thickness of 11 nm with average dimensions (length × width) of 64 × 38 nm and there is very few small sized {001}-TiO_2 (Fig. 3d). Fig. 3e shows the TEM image of {001}-TiO_2/MoS_2/RGO. The {001}-TiO_2 nanosheets and MoS_2/RGO can be observed clearly. The HRTEM image of Fig. 3f shows that the lattice spacing of 0.35 nm and 0.62 nm can be assigned to (101) planes of MoS_2 and (101) planes of anatase {001}-TiO_2, respectively.

3.2 Photocatalytic study

The photocatalytic activity of all the as-prepared samples was evaluated from measurements on the degradation of Rh B. Before illumination, the suspensions were prepared *via* stirring in dark for 30 minutes, such that they reached the adsorption–desorption equilibrium.

In this study, firstly, we investigate the optimum ratio of MoS_2 and RGO in a co-catalyst, as shown in Fig. 4a. The weight percentage of MoS_2/RGO in the hybrid is kept at 7 wt%, and the {001}-TiO_2/MoS_2/RGO hybrid with a MoS_2 : RGO ratio of 97 : 3 wt% shows the highest photodegradation rate. Then we studied the influence of the species and contents of co-catalyst on the photodegradation activity. As shown in Fig. 4c, the color dye without catalyst presents no photodegradation activity under visible light irradiation. It verifies that self-sensitisation couldn't cause the degradation. The pure {001}-TiO_2 exhibits a low photocatalytic activity which could be caused by the rapid recombination of the CB electrons and the VB holes. While by

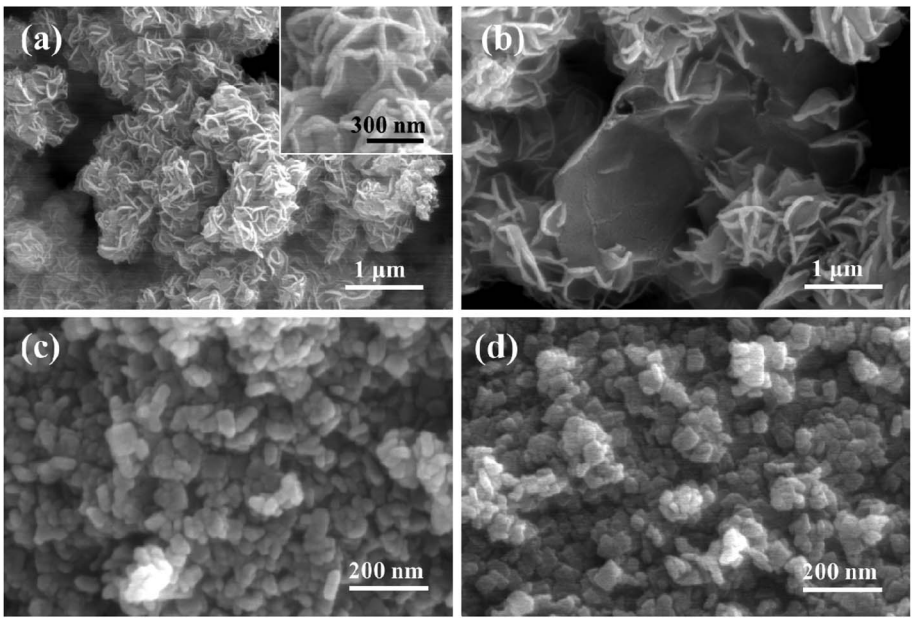

Fig. 2 SEM images of MoS_2 (a), MoS_2/RGO (b), TiO_2 (c) and {001}-TiO_2/MoS_2/RGO (d).

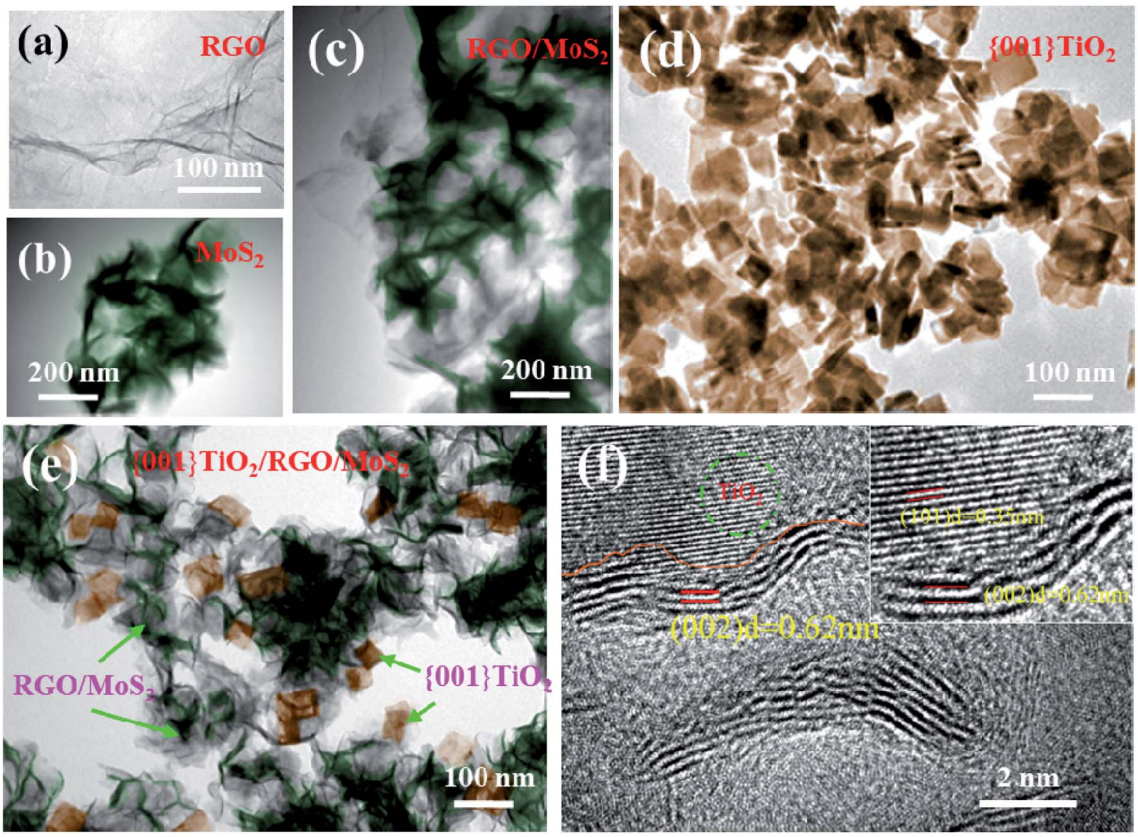

Fig. 3 TEM images of RGO (a), MoS_2 (b), MoS_2/RGO (c), {001}-TiO_2 (d), {001}-TiO_2/MoS_2/RGO (e); HRTEM image of {001}-TiO_2/MoS_2/RGO (f).

the incorporation of MoS_2, the photocatalytic activity of {001}-TiO_2 is enhanced significantly, which is caused by the transfer of electrons from {001}-TiO_2 to MoS_2.[43] In fact, the {001}-TiO_2/MoS_2 hybrid have exhibited excellent performance for the adsorption of Rh B under dark condition (as shown in Fig. S5c–f†). Through the incorporation of MoS_2/RGO as the co-catalyst for {001}-TiO_2, the photocatalytic activity of the hybrid could be further improved, as demonstrated in Fig. 4b, the {001}-TiO_2/0.07(MoS_2/0.03RGO) hybrids show the best photocatalytic performance. UV-visible investigation shows that after 60 min of visible light ($\lambda > 400$ nm) irradiation, 92.3% of Rh B has been degraded by {001}-TiO_2/0.07(MoS_2/0.03RGO) (as shown in Fig. 4d). It is suggested that the enhanced separation of photogenerated electrons and holes because of the high electron conductivity of RGO could result in the enhanced photocatalytic performance. In addition, the photocatalytic performance of {001}-TiO_2/0.07(MoS_2/0.03RGO) catalyst can also be evaluated by TOC removal. As shown in Fig. S5b,† the{001}-TiO_2/0.07(MoS_2/0.03RGO) hybrid catalyst shows the highest TOC removal rate of Rh B, which basically coincides with the result of the degradation rate, illustrating that the Rh B has been thoroughly mineralized. The color change of Rh B solution also reflects the efficiency of catalyst. We can clearly observe that the Rh B solution under the photocatalytic degradation of {001}-TiO_2/MoS_2/RGO hybrid is close to white (as shown in Fig. S4†).

The reaction kinetics of Rh B reduction is determined by plotting the value of $\ln(C_0/C)$ *versus* illumination time, and the reaction rate constants (K) are calculated by the pseudo-first order model. As shown in Fig. S5a,† the values of K for {001}-TiO_2, {001}-TiO_2/RGO, {001}-TiO_2/MoS_2 and {001}-TiO_2/MoS_2/RGO are 0.0084, 0.0201, 0.01285 and 0.03325, respectively. It can be seen that the {001}-TiO_2/MoS_2/RGO hybrid photocatalyst exhibits the highest rate (0.03325) of photodegradation.

The stability and reusability of {001}-TiO_2/MoS_2/RGO were also evaluated. Fig. S1b† shows the XRD patterns of {001}-TiO_2/MoS_2/RGO before and after photocatalysis, and it is observed that after photocatalysis the crystal structure has not changed. The inset of Fig. S5b† illustrates that the photocatalytic activity of {001}-TiO_2/MoS_2/RGO displays a slight decrease after running for five successive cycles, indicating that the {001}-TiO_2/MoS_2/RGO hybrid is stable and efficient photocatalyst.

3.3 Mechanisms of the enhanced photocatalytic activity

It is well known that the photocatalytic activity of semiconductive photocatalysts is intrinsically governed by three processes: (i) photoexcitation of semiconductor to generate electron–hole pairs, (ii) charge separation and diffusion to the surface of the catalysts, and (iii) surface activation for redox reactions.[38] In the sections that follow, the mechanisms of the enhanced photocatalytic performance of {001}-TiO_2/MoS_2/RGO

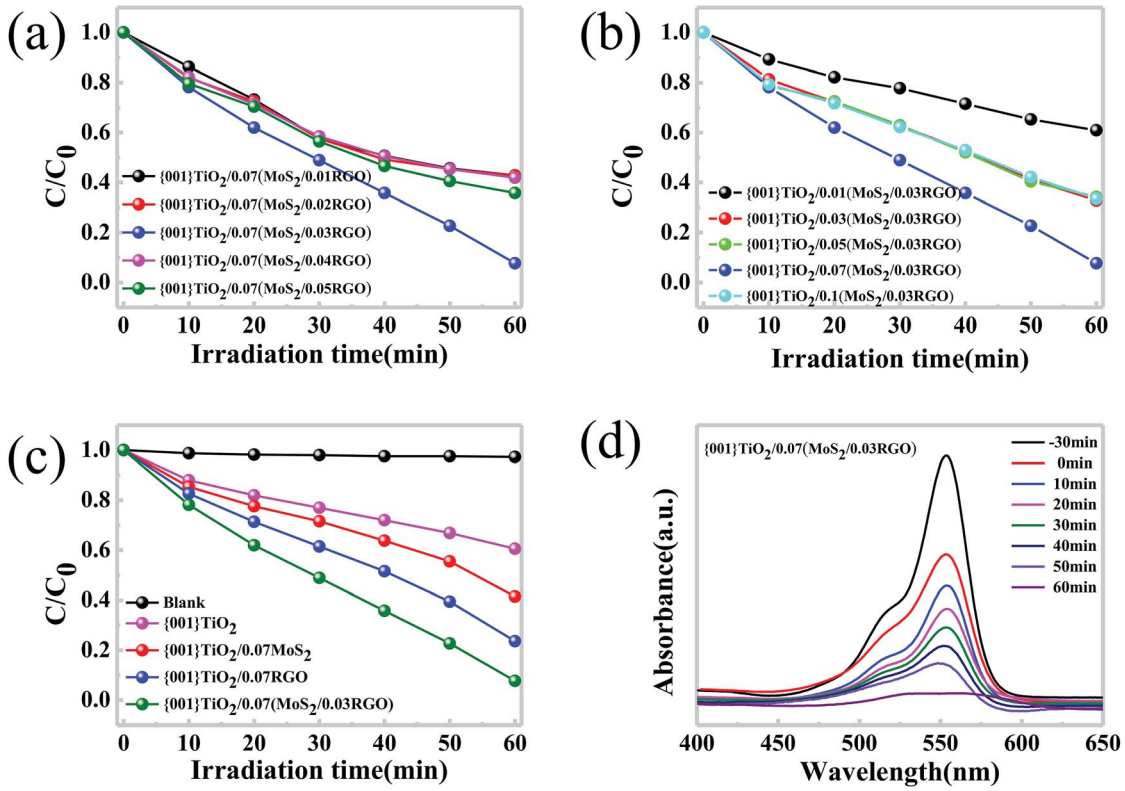

Fig. 4 Photocatalytic degradation of Rh B under visible light irradiation over (λ > 400 nm) (a) {001}-TiO_2/MoS_2/RGO with different RGO percentages; (b) {001}-TiO_2/MoS_2/RGO with different contents of MoS_2/0.03RGO; (c) blank, {001}-TiO_2, {001}-TiO_2/0.07GO, {001}-TiO_2/0.07MoS_2 and {001}-TiO_2/0.07(MoS_2/0.03RGO). (d) UV-visible spectra of {001}-TiO_2/MoS_2/RGO.

are elucidated separately based on the abovementioned processes.

The UV-vis diffuse reflectance spectra of TiO_2 and {001}-TiO_2/MoS_2/RGO are shown in Fig. 5a. Compared with pure {001}-TiO_2, the {001}-TiO_2/MoS_2/RGO hybrid shows an enhanced visible light absorption. The band gaps of {001}-TiO_2 and {001}-TiO_2/MoS_2/RGO are determined to be 3.2 and 3.04 eV, respectively, according to the onset of the absorption edge. The {001}-TiO_2/MoS_2/RGO hybrid exhibits a narrower band gap and higher absorption intensity, meaning that their redox potentials as well as the recombination of electrons and holes are reduced as compared with those of {001}-TiO_2.[47]

Fig. 5b shows the nitrogen adsorption/desorption isotherms of {001}-TiO_2 and {001}-TiO_2/MoS_2/RGO. The isotherms for pure {001}-TiO_2 reveal a type-IV isotherm with an H3 hysteresis loop, which indicates that the holes are formed by the accumulation of flaky particles. The {001}-TiO_2/MoS_2/RGO hybrids display a type-IV isotherm with an H4 hysteresis loop, suggesting the slit-shaped pores are produced by the layered structure. Based on BET calculation, the surface area of {001}-TiO_2 is 111.124 $m^2\ g^{-1}$ and the surface area of {001}-TiO_2/MoS_2/RGO is 76.123 $m^2\ g^{-1}$, revealing the information on their microstructures consistent with those observed in SEM images (Fig. 2c and d).

It is revealed that graphene could improve the photocatalytic property of {001}-TiO_2/MoS_2/RGO hybrid owning to the fact that graphene can rapidly transfer electrons to hinder the recombination of photogenerated electron–hole pairs. We can evaluate the probability of recombination of electron–hole pairs by PL spectroscopy, in that the higher fluorescence intensity represents higher probability of recombination. Fig. 5c shows the PL spectra under 400 nm excitation wavelengths for pure {001}-TiO_2 and {001}-TiO_2/MoS_2/RGO samples, and a strong emission peak appears at about 602 nm.[48] It is found that the PL intensity of {001}-TiO_2/MoS_2/RGO sample is lower than that of pure {001}-TiO_2, which indicates that by the incorporation of MoS_2/RGO co-catalyst, the hybrid can inhibit the recombination of excited electrons and holes in the {001}-TiO_2/MoS_2/RGO catalysts. The resistance of catalyst is determined by the electrochemical impedance spectroscopy (ESI). Fig. 5d shows the ESI spectrogram of {001}-TiO_2 and {001}-TiO_2/MoS_2/RGO. Compared with pure {001}-TiO_2, the {001}-TiO_2/MoS_2/RGO hybrid presents a smaller frequency semicircle, suggesting the resistance of {001}-TiO_2/MoS_2/RGO is lower than that of {001}-TiO_2. Thus, it can be concluded that the introduction of MoS_2/RGO co-catalysts into {001}-TiO_2 can reduce the recombination of charge carriers, which is consistent with the results of PL spectrum.

The schematic of photocatalytic enhancement and electron transfer of {001}-TiO_2/MoS_2/RGO is shown in Fig. 5e. Under visible light irradiation, the VB electrons of MoS_2 and {001}-TiO_2 are excited to the CB, leaving holes (h^+) in the VB.[49,50]

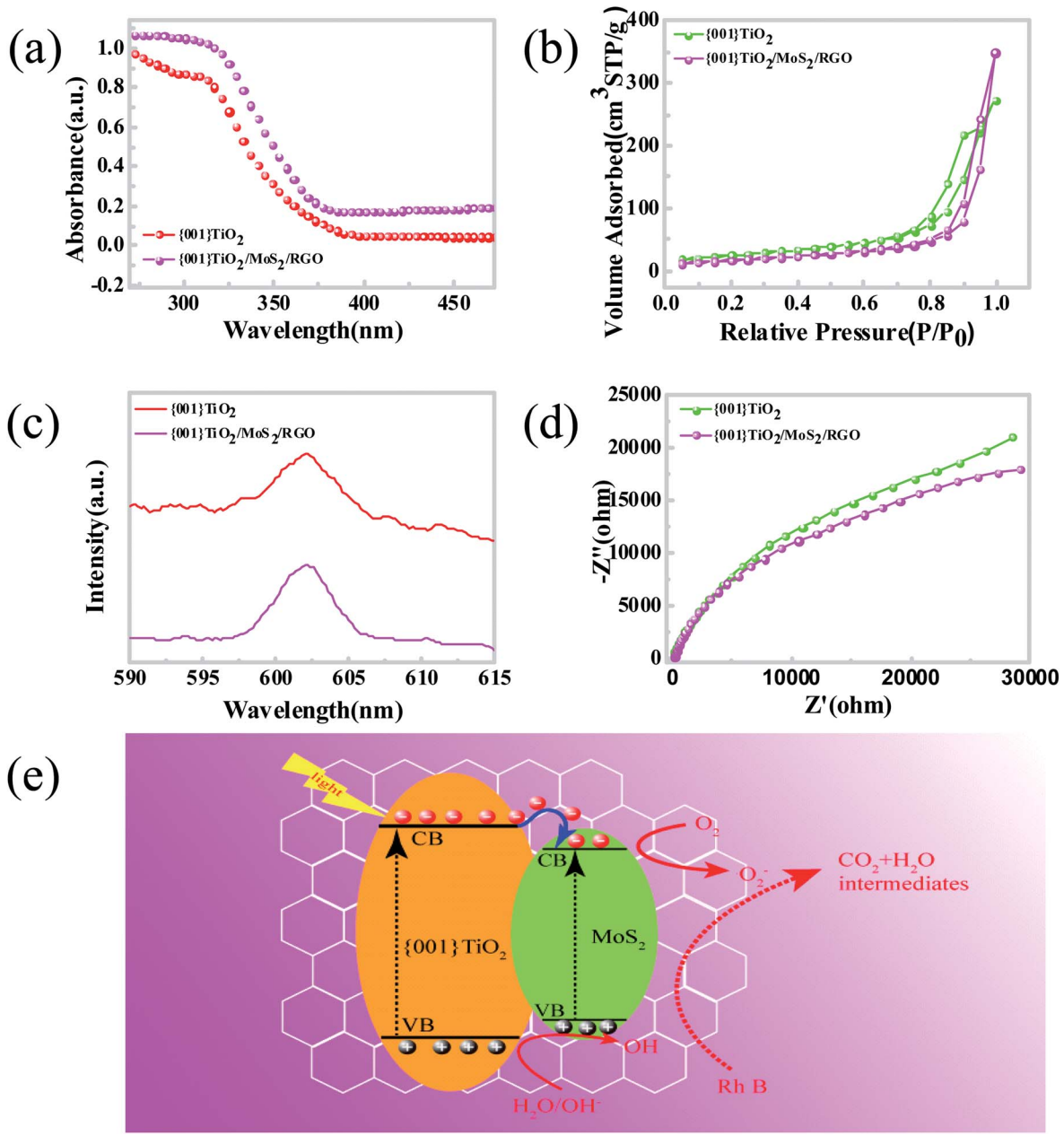

Fig. 5 (a) UV-vis diffusive reflectance spectra of pure {001}-TiO_2 and {001}-TiO_2/MoS_2/RGO; the inset is corresponding plot of the transformed Kubelka–Munk function *versus* the energy of light; (b) N_2 adsorption/desorption isotherms of pure {001}-TiO_2 and {001}-TiO_2/MoS_2/RGO; (c) PL spectra of pure {001}-TiO_2 and {001}-TiO_2/MoS_2/RGO under 400 nm excitation wavelength; (d) electrochemical impedance spectroscopy (EIS) Nyquist plots of the sample electrodes which are made from the pure {001}-TiO_2 and {001}-TiO_2/MoS_2/RGO treated with visible light (λ > 400 nm) irradiation; (e) schematic diagram for photocatalytic mechanism of {001}-TiO_2/MoS_2/RGO.

Meanwhile, the photoinduced electrons of {001}-TiO_2 can transfer to MoS_2 *via* the conductive network of RGO. It is worth noting that the separation of photogenerated electron–hole pairs of {001}-TiO_2/MoS_2/RGO is more rapid than that of conventional TiO_2/MoS_2/RGO owing to the especially reactive {001} facets of anatase TiO_2. The photogenerated electrons on the CB of samples can react with O_2 to produce superoxide radical anions $\cdot O_2^-$. Meanwhile those photoexcited holes on the VB of samples react with H_2O and hydroxide ions to generate ·OH radicals. The powerful oxidizing agents $\cdot O_2^-$ and ·OH could effectively decompose the Rh B into CO_2, H_2O or other intermediates. As listed in Table 1, we have compared {001}-TiO_2/MoS_2/RGO with other representative composites reported in literature. It can be found that the {001}-TiO_2/MoS_2/RGO exhibits desirable catalytic performance, which rapid and effective, indicating the promising perspective of {001}-TiO_2/MoS_2/RGO in the removal of pollutants applications.

Table 1 Catalytic activity of representative composites

Catalyst	Method	Degradation (%)	Degradation target	Times (min)	Ref.
{001}-TiO_2/MoS_2/RGO	Hydrothermal	92.3	Rhodamine B	60	This work
$BiPO_4$/MoS_2/RGO	Hydrothermal	92	Rhodamine B	90	51
Bi_2WO_6/MoS_2/RGO	Hydrothermal	92	Rhodamine B	180	48
TiO_2/RGO	Hydrothermal	94	Rhodamine B	120	52
CeO_2/SnO_2/rGO	Hydrothermal	95	Methylene blue	90	53
rRGO–ZnO–MoS_2	Hydrothermal	90	Methylene blue	75	54
$NiWO_4$–ZnO–NRGO	Microwave irradiation method	89	Methylene blue	120	55
{001}-TiO_2/RGO	Hydrothermal	82	Methylene blue	60	48
TiO_2/RGO/Ag	Sol–gel process photo-assisted reduction method	93	Methylene blue	120	56
rGO–$ZnWO_4$–Fe_3O_4	Microwave irradiation method	97	Methylene blue	135	57
TiO_2/MoS_2/RGO	Hydrothermal	97	Methylene blue	100	49

4. Conclusion

In summary, we have successfully synthesized the {001}-TiO_2/MoS_2/RGO hybrids with effective catalytic performance using a facile hydrothermal method. The {001}-TiO_2/MoS_2/RGO photocatalysts with 7 wt% MoS_2/RGO co-catalyst show the highest photodegradation activity for the degradation of Rh B under visible light irradiation (λ > 400 nm). The {001} facets of {001}-TiO_2/MoS_2/RGO accelerate the separation of photogenerated electron–hole pairs, and RGO rapidly transfer the photoinduced electrons from {001}-TiO_2 to MoS_2, which further enhances the charge carrier separation of the {001}-TiO_2/MoS_2/RGO hybrid. It is believed that such synergy effect promotes the photocatalytic performance of {001}-TiO_2/MoS_2/RGO hybrids. Taking into account their facile synthesis route and excellent photocatalytic performance, the MoS_2/RGO hybrids are promising co-catalyst which can be widely used for co-photocatalysts and {001}-TiO_2/MoS_2/RGO hybrids are promising candidates for photocatalytic degradation of Rh B.

Conflicts of interest

There is no conflict in the statement.

Acknowledgements

This work was supported by Province Advantages and Distinctive Subjects Project of Heilongjiang (YSTSXK201810), Heilongjiang Provincial Education Department Project (LTSW201738), Qiqihar City Science and Technology Project (SFGG-201601), the Innovation Fund Project for Graduate Student of Qiqihar University (YJSCX2017-022X).

References

1 M. R. Hoffmann, W. Choi and D. W. Bahnemann, *Chem. Rev.*, 1995, **95**, 69–96.
2 N. Serpone and A. V. Emeline, *J. Phys. Chem. Lett.*, 2012, **3**, 673–677.
3 P. K. J. Robertson, J. M. C. Robertson and D. W. Bahnemann, *J. Hazard. Mater.*, 2012, **211**, 161–171.
4 H. Kisch, *Angew. Chem., Int. Ed.*, 2013, **52**, 812–847.
5 S. P. Albu, A. Ghicov, J. M. Macak and P. Schmuki, *Nano Lett.*, 2007, **7**, 1286–1289.
6 T. Tachikawa, M. Fujitsuka and T. Majima, *J. Phys. Chem. C*, 2007, **111**, 5259–5275.
7 J. Zhang, Q. Xu, Z. C. Feng, M. J. Li and C. Li, *Angew. Chem., Int. Ed.*, 2010, **47**, 1766–1769.
8 M. M. Khan, S. A. Ansari, D. Pradhan and M. Omaish, *J. Mater. Chem. A*, 2013, **2**, 637–644.
9 J. Schneider, M. Matsuoka, M. Takeuchi, J. Zhang, Y. Horiuchi, M. Anpo and D. W. Bahnemann, *Chem. Rev.*, 2014, **114**, 9919–9986.
10 R. Kaplan, B. Erjavec, G. Dražić, J. Grdadolnik and A. Pintar, *Appl. Catal., B*, 2015, **181**, 465–474.
11 H. Choi, A. Sofranko and D. Dionysiou, *Adv. Funct. Mater.*, 2010, **16**, 1067–1074.
12 T. Fotiou, T. M. Triantis, T. Kaloudis, K. E. O'Shea, D. D. Dionysiou and A. Hiskia, *Water Res.*, 2016, **90**, 52–61.
13 J. B. Joo, Q. Zhang, M. Dahl and I. Lee, *Energy Environ. Sci.*, 2012, **5**, 6321–6327.
14 J. B. Joo, I. Lee, M. Dahl and G. D. Moon, *Adv. Funct. Mater.*, 2014, **23**, 4246–4254.
15 J. Wang, Z. Wang, H. Li, Y. T. Cui and Y. C. Du, *J. Alloys Compd.*, 2010, **494**, 372–377.
16 F. Li, J. Xu, L. Chen and B. B. Ni, *J. Mater. Chem. A*, 2012, **1**, 225–228.
17 X. Dong, J. Tao, Y. Y. Li, T. Wang and H. Zhu, *Acta Phys.-Chim. Sin.*, 2009, **25**, 1874–1882.
18 J. C. Liu, L. Liu, H. G. Bai, Y. J. Wang and D. D. Sun, *Appl. Catal., B*, 2011, **106**, 76–82.
19 S. D. Perera, R. G. Mariano, K. Vu and N. Nijem, *ACS Catal.*, 2012, **2**, 949–956.
20 Y. Zhang, N. Zhang, Z. R. Tang and Y. J. Xu, *Phys. Chem. Chem. Phys.*, 2012, **14**, 9167–9175.
21 N. Zhang, S. Liu, X. Fu and Y. J. Xu, *J. Phys. Chem. C*, 2011, **115**, 9136–9145.
22 R. Liu, P. Wang, X. Wang, H. Yu and J. G. Yu, *J. Phys. Chem. C*, 2012, **116**, 17721–17728.
23 R. Asahi, T. Morikawa, H. Irie and T. Ohwaki, *Chem. Rev.*, 2014, **114**, 9824–9852.
24 D. Qu, M. Zheng, P. Du, Y. Zhou, L. Zhang, D. Li, H. Q. Tan, Z. Zhao, Z. G. Xie and Z. C. Sun, *Nanoscale*, 2013, **5**, 12272–12277.

25 A. Kubacka, M. Ferrer, M. Fernandezgarcia, C. Serrano, M. Cerrada and M. Fernández-García, *Appl. Catal., B*, 2011, **104**, 346–352.
26 Y. Jiang, W. F. Chen, P. Koshy and C. C. Sorrell, *J. Mater. Sci.*, 2019, **54**, 5266–5279.
27 S. Liu, N. Zhang, Z. R. Tang and Y. J. Xu, *ACS Appl. Mater. Interfaces*, 2012, **4**, 6378–6385.
28 M. Wang, L. Sun, Z. Lin and J. H. Cai, *Energy Environ. Sci.*, 2013, **6**, 1211–1220.
29 Z. A. Huang, Q. Sun, K. L. Lv, Z. H. Zhang, M. Li and B. Li, *Appl. Catal., B*, 2015, **164**, 420–427.
30 X. Lin, D. Xu, Y. Xi, R. Zhao, L. N. Zhao, M. S. Song, H. J. Zhai, G. B. Che and L. M. Chang, *Colloids Surf., A*, 2017, **513**, 117–124.
31 Y. Z. Hong, E. L. Liu, J. Y. Shi, X. Lin, L. Z. Sheng, M. Zhang, L. Y. Wang and J. H. Chen, *Int. J. Hydrogen Energy*, 2019, **44**, 7194–7204.
32 H. Zeng, J. Dai, W. Yao, D. Xiao and X. Cui, *Nat. Nanotechnol.*, 2012, **7**, 490–493.
33 Y. Li, H. Wang, L. Xie, Y. Liang, G. Hong and H. Dai, *J. Am. Chem. Soc.*, 2011, **133**, 7296–7299.
34 Z. Yin, H. Li, H. Li, L. Jiang, Y. Shi, Y. Sun, G. Lu, Q. Zhang, X. Chen and H. Zhang, *ACS Nano*, 2012, **6**, 74–80.
35 M. A. Lukowski, A. S. Daniel, F. Meng, A. Forticaux, L. S. Li and S. Jin, *J. Am. Chem. Soc.*, 2013, **135**, 10274–10277.
36 U. Gupta, B. S. Naidu, U. Maitra, A. Singh, S. N. Shirodkar, U. V. Waghmare and C. N. R. Rao, *APL Mater.*, 2014, **2**, 092802.
37 X. Hu, H. Zhao, J. Tian, J. X. Gao, Y. J. Li and H. Z. Cui, *Sol. Energy Mater. Sol. Cells*, 2017, **172**, 108–116.
38 S. Bai, L. Wang, X. Chen, J. t. Du and Y. j. Xiong, *Nano Res.*, 2015, **8**, 175–183.
39 W. C. Peng, Y. Chen and X. Y. Li, *J. Hazard. Mater.*, 2016, **309**, 173–179.
40 S. Liu, J. Yu and M. Jaroniec, *J. Am. Chem. Soc.*, 2010, **132**, 11914–11916.
41 J. Pan, G. Liu, G. Q. Lu and H. M. Cheng, *Angew. Chem., Int. Ed.*, 2011, **123**, 2181–2185.
42 N. Roy, Y. Sohn and D. Pradhan, *ACS Nano*, 2013, **7**, 2532–2540.
43 D. Q. Zhang, J. X. Chai, J. Y. Cheng, X. Y. Yang, H. Wang, Z. L. Zhao, C. Han, G. C. Shan, W. J. Zhang, G. P. Zheng and M. S. Cao, *Appl. Surf. Sci.*, 2018, **462**, 872–882.
44 O. Akhavan, *Carbon*, 2015, **81**, 158–166.
45 W. S. Wang, D. H. Wang, W. G. Qu, L. Q. Lu and A. W. Xu, *J. Phys. Chem. C*, 2012, **116**, 19893–19901.
46 W. L. Song, X. T. Guan, L. Z. Fan, W. Q. Cao, C. Y. Wang and M. S. Cao, *Carbon*, 2015, **93**, 151–160.
47 X. Liang, B. Quan, G. B. Ji, W. Liu, H. W. Zaho, S. S. Dai, J. Lv and Y. W. Du, *ACS Sustainable Chem. Eng.*, 2017, **5**, 10570–10579.
48 M. Liu, X. Xue, S. S. Yu, X. Y. Wang, Xi. Y. Hu, H. W. Tian, H. Chen and W. T. Zheng, *Sci. Rep.*, 2017, **7**, 3637.
49 C. B. Liu, L. L. Wang, Y. H. Tang, S. L. Luo, Y. T. Liu, S. Q. Zhang, Y. X. Zeng and Y. Z. Xu, *Appl. Catal., B*, 2015, **164**, 1–9.
50 D. B. Nimbalkar, H. H. Lo, P. V. R. K. Ramacharyulu and S. Y. C Ke, *RSC Adv.*, 2016, **6**, 31661–31667.
51 H. Lv, Y. M. Liu, H. B. Tang, P. Zhang and J. J. Wang, *Appl. Surf. Sci.*, 2017, **425**, 100–106.
52 F. Wang and K. Zhang, *J. Mol. Catal. A: Chem.*, 2011, **345**, 101–107.
53 A. Priyadharsan, V. Vasanthakumar, S. Karthikeyan, V. Raj, S. Shanavas and P. M. Anbarasan, *J. Photochem. Photobiol., A*, 2017, **346**, 32–45.
54 A. Priyadharsan, S. Shanavas and V. Vasanthakumar, *Colloids Surf., A*, 2015, **559**, 43–53.
55 M. M. J. Sadiq, U. S. Shenoy and D. K. Bhat, *J. Phys. Chem. Solids*, 2017, **109**, 124–133.
56 H. W. Tian, C. X. Wan, X. Xue and X. Xin, *Catalysts*, 2017, **7**, 156.
57 M. M. Ja, U. Sandhya and D. K. Bhat, *RSC Adv.*, 2016, **6**, 61821–61829.